International Journal of Impact Engineering 184 (2024) 104809

Contents lists available at ScienceDirect

International Journal of Impact Engineering

journal homepage: www.elsevier.com/locate/ijimpeng

Crashworthiness and dimensional stability analysis of zero Poisson's ratio Fish Cells lattice structures

Ashutosh Jha, Guglielmo Cimolai, Iman Dayyani *

Centre for Aeronautics, School of Aerospace, Transport and Manufacturing, Cranfield University, MK43 0AL, UK

ARTICLE INFO

Keywords:
Fish Cells
Sandwich structures
Zero Poisson's ratio (ZPR)
Finite elements
Impact analysis
Dimensional stability

ABSTRACT

The present article introduces Zero Poisson's Ratio (ZPR) Fish Cells metamaterial and investigates the effects of Poisson's ratio on the crashworthiness of Positive (PPR), Negative (NPR), and Zero Poisson's ratio lattice structures. High-fidelity Finite Element (FE) models of the proposed sandwich structures are built, based on identical domains for unit cells. Impact performances of lattice structures are addressed for low (2 m/s) and high (5 m/s) impact velocities in three orthogonal directions. The parameters investigated for crashworthiness include impactor's penetration depth, von Mises stress distribution, edges deformation and dimensional stability. Numerical results demonstrate that, unlike PPR and NPR models, the Fish Cells ZPR model possesses greater lateral stability and structural integrity with minimal edge deformations in all three directions. This leads to reduced lateral impact transfer to adjacent components and localised damaged zones, increasing the life span of structural components while reducing maintenance and repair downtime. Experimental analyses are conducted on the Fish Cells metamaterial through a drop tower test for demonstrating agreement with simulations and validation of the proposed modelling approach.

1. Introduction

Mechanical metamaterials are a typology of architected materials based on a rational microscale design that permits the achievement of exceptional mechanical behaviours not available in naturally originated ones [1,2]. Examples of exotic properties include, for example, ultra-high stiffness [3], tailored Poisson's ratio [4], etc. Such properties result from the careful design of small-scale, periodically repeating unit-cell elements, rather than from the base material used [5]. As such, the field of mechanical metamaterials offers a wide range of possibilities in automotive, aerospace, and other industries where weight reduction plays a critical role. Within the decade of their discovery, metamaterials have taken the centre stage in many applications, yet the nature of these materials is still not completely defined, offering therefore numerous chances for further explorations.

Based on their Poisson's ratio behaviour under large strains, mechanical metamaterials can be classified into Positive Poisson's Ratio (PPR), Negative Poisson's Ratio (NPR), or auxetics, and Zero Poisson's Ratio (ZPR) metamaterials [6,7]. As an example of their differences, the work of Grima et al. [6] has compared the performances of PPR, NPR and ZPR metamaterials in the context of geometric conformability over curved surfaces.

PPR metamaterials include conventional hexagonal honeycomb unit cells, vastly used in engineering applications thanks to their lightweight properties and tailorable mechanical performances [8,9]. Honeycomb structures with PPR behaviour show anticlastic or saddle-shaped curvatures if stressed with out-of-plane bending loads [10,11]. Recent work performed on hexagonal cellular structures has developed the performances of such lattice topology. Liu et al. [12] studied a three-dimensional model for the flatwise compressive properties of Nomex hexagonal cores considering the effect of debonding imperfections in the unit cell elements. Sun et al. [13] studied the compressive properties of honeycomb sandwich structures with reinforced hexagonal cores. Wang et al. [14] have discussed the mechanical behaviours of honeycomb structures under out-of-plane compressive loading through numerical simulation and experimental analyses. Tao et al. [15] have proposed a novel graded honeycomb structure with gradient-based hexagonal cellular materials and studied its dynamic behaviour when subjected to out-of-plane compression through finite element simulation.

For large-strain ZPR metamaterials, the need is to have a constant ZPR behaviour over a large strain range for morphing applications being

* Corresponding author.
E-mail address: I.Dayyani@Cranfield.ac.uk (I. Dayyani).

https://doi.org/10.1016/j.ijimpeng.2023.104809
Received 5 June 2023; Received in revised form 22 August 2023; Accepted 20 October 2023
Available online 28 October 2023

affected by tessellation geometry, deformation mechanism and original constituent material. Additionally, cellular structures with zero Poisson's ratio do not exhibit synclastic or anticlastic curvature when bent out-of-plane. Ren et al. [16] developed an elastomer skin that showed ZPR behaviour for up to 25% strain which was limited by the ultimate strain of the elastomer material. The mechanism employed pure tensile stretching as its inherent deformation mechanism. Liu et al. [17] introduced a filamentary microstructure intending to maximise the strain range of the soft network materials. They reported constant ZPR behaviour for up to a strain range of 60%. Yang and Ma proposed 2D architected mechanical metamaterials whose tensile mechanical response can be tailored by harnessing snap-through instabilities. Based on their 2D double-U architecture, a 3D ZPR mechanical metamaterial was developed which exhibited ZPR behaviour for up to 200% and 67% under tension and compression, respectively [18]. Moreover, Naghavi Zadeh et al. [19] introduced the Fish Cells metamaterial, which is made up of a combination of Honeycomb (PPR) and Re-entrant (NPR) unit cells to achieve ZPR behaviour. As the Fish Cells metamaterial has not yet been applied in sandwich structures, a major novelty of this paper resides in its analysis for impact applications.

Metamaterials with NPR behaviour are also indicated as auxetics [20]. Re-entrant honeycomb structures possess auxetic properties, and compared with conventional hexagonal honeycombs, the auxetic configurations feature compliant in-plane shear and enhanced indentation resistance [21]. Contrary to the PPR honeycomb structures, if the in-plane Poisson's ratio of the honeycomb structure is negative as in the case of re-entrant unit cells, the curvatures are synclastic and result in a dome-shaped bent structure. Subramani et al. [22] have developed auxetic structures based on braided composites using re-entrant hexagonal unit cells as basic structures. Jin et al. [23] have proposed an innovative sandwich structure with re-entrant hexagonal cell cores and assessed numerically its dynamic performance and blast resistance under explosion. Hou et al. [24] have described experimental tests of graded conventional/auxetic honeycomb cores manufactured using Kevlar woven fabric / 914 epoxy prepreg under compression loading. The bending performances of the honeycomb structures with PPR or NPR however limit their applications in cylindrical bending morphing engineering [25].

Mechanical metamaterials and other types of lattice materials have been successfully implemented in energy absorption structures and energy dissipation applications, for example improving crashworthiness properties of aeroplanes and road vehicles [26,27]. As they can sustain significant compressive strains with low stresses involved, architected metamaterials can absorb a high amount of energy without failure in compression. Energy absorption in a lattice structure is due to their ability to transform the impactor's kinetic energy into elastic-plastic deformation and eventually fracture of the constituent unit cells elements [28,29]. In recent years, impact tests have been conducted on mechanical metamaterials with different purposes. Sarvestani [30] analysed available sandwich cores with six-sided polygons and their abilities on absorbing energies during low-velocity impacts, through numerical and experimental analyses. He found that Poisson's ratio value plays a key role in determining the abilities of a panel core to withstand impacts. Tan et al. [31] investigated a reusable steel-based metamaterial able to dissipate energy through plastic deformation and inelastic instability. The structure's repeatability was examined through cyclic testing and results revealed that the proposed structure is repeatable, although increasing the dimensions reduces such property.

The availability of additive manufacturing technologies, such as 3D printing has made it possible to evaluate experimentally the behaviour of advanced mechanical metamaterials and architected cellular cores for elastic-plastic deformation [32]. Bates et al. [33] evaluated the energy absorption behaviour of a 3D-printed honeycomb structure made of thermoplastic polyurethanes. Habib et al. [34] performed experimental and numerical analyses on the energy absorption and compressive fracture properties of 3D printed PPR honeycomb under in-plane uniaxial loading with varying wall thicknesses, finding that the plastic deformation mechanisms of regular hexagonal cellular structures are different in two perpendicular in-plane directions. Sarvestani et al. [35] addressed the out-of-plane and in-plane mechanical properties and energy absorption capability of lightweight sandwich structures with different cellular cells, finding that the auxetic sandwich panel exhibited better energy absorption characteristics. Xu et al. [36] assessed the energy absorption capability of a hybrid structure based on regular hexagonal and auxetic unit cells through in-plane compression loading. Experimental results based on 3D printed samples demonstrated that the proposed metamaterial possesses superior energy absorption performances compared to the regular hexagonal lattice structure. Moreover, Namvar et al. [37] evaluated the energy absorption characteristics of auxetic, hexagonal and aux-hex structures employing a shape memory 4D printing, confirming that metamaterial with re-entrant auxetic unit-cells shows superior energy absorption capabilities.

Although prior publications have focused on addressing the mechanical capabilities of PPR, NPR and in some instances ZPR metamaterial lattice structures, discussions on their crashworthiness characteristics and energy absorption behaviours are still open to more profound studies. This is especially true in the context of edge deformations, lateral stability, and the damage extent of metamaterial lattice under localised impact loading. As such, the need for a clearer comparison of metamaterial sandwich structures' behaviours under impact and their dependency on Poisson's ratio is identified. Additionally, the recently discovered ZPR Fish Cells structure has never been modelled as a lattice structure nor has been tested for impact behaviour. To cover these research questions, the present paper aims to address the impact behaviour of three different metamaterial cores, i.e. Honeycomb (PPR), Fish Cells (ZPR) and Re-entrant (NPR). Moreover, three different unit cell propagation patterns have been considered for both high and low impact velocities.

The paper is organized as follows: Section 2 presents the considered unit cell's structures, with their geometric parameters, associated material properties, and impact directions. Moreover, Finite Element (FE) models of the impactor and lattice structure are carefully described. Section 3 presents results from the numerical simulations conducted in Abaqus/Explicit, where maximum penetration depth, force-displacement characteristics, and von Mises stress distribution are reported for the considered geometries and impact velocities. Section 4 includes a further discussion of the presented numerical results, while Section 5 reports an experimental validation conducted on 3D-printed test samples of the Fish Cells' lattice structure through a drop tower test. A comparison between numerical and experimental results is undertaken to validate the proposed methodology, and several conclusions are drawn.

2. Problem definition

In this section, the three different unit cells under study, i.e., Fish Cells (ZPR), Honeycomb (PPR), and Re-entrant (NPR), are introduced followed by their geometric parameters, their material characterisation, as well as a mesh sensitivity study and Finite Element (FE) modelling details.

Fig. 1 shows the unit cells in 2D planar and 3D orthotropic projections, along with their geometric definitions. For consistency of results, the height (H) and the length (L_{uc}) of the unit cells are kept constant. Two in-plane (D1 and D2) and one out-of-plane (D3) directions are considered for impact analyses.

2.1. Material characterization

Aluminium alloy Al5083-H116 has been considered as the constituent material of the proposed unit cells due to its high energy absorption properties and its lightweight characteristics, which make it suitable for crashworthiness applications in the aerospace and automotive fields.

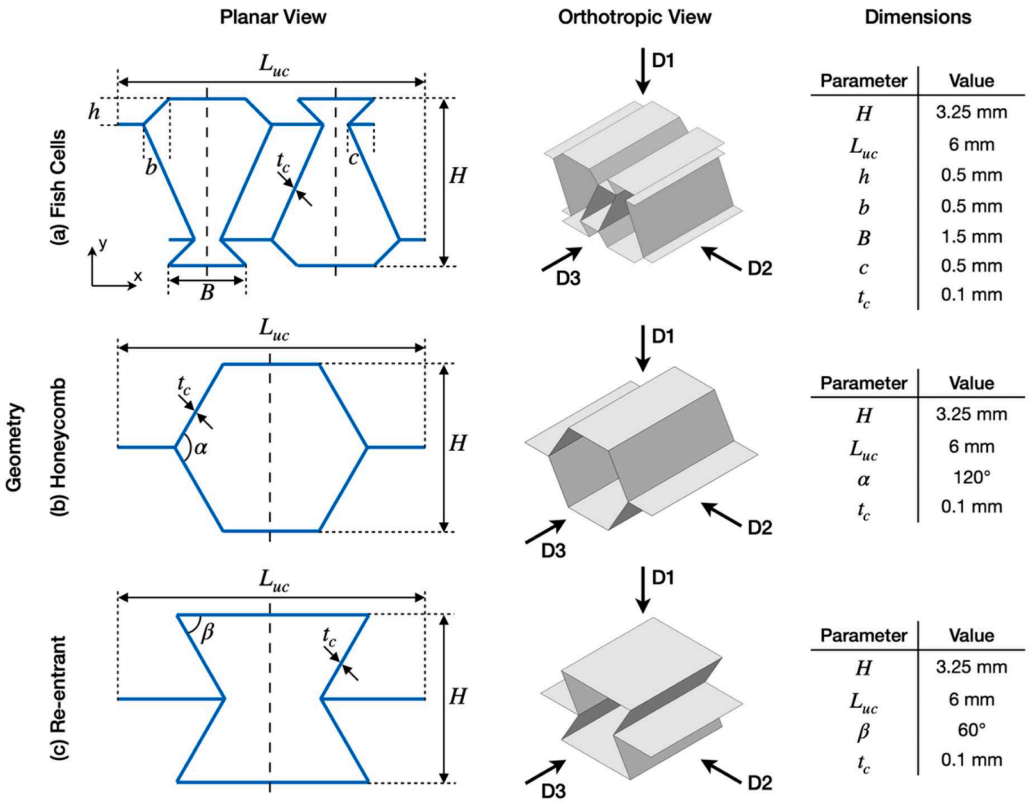

Fig. 1. Planar and orthotropic views of the unit cell geometries with geometric definitions and impact directions.

For the implementation in a FE environment, its mechanical behaviour is modelled using Johnson-Cook elastic-plastic model, with the material characterization data collected in Table 1. J-C plasticity model [38] is an empirical model used to describe the plastic behaviour of ductile metals under large deformations, considering strain rate and temperature effects acting on the material. Flow stress can be determined from Eq. (1), as a function of the strain hardening effect, the strain rate strengthening effect and the temperature effect on the material plastic behaviour:

$$\sigma(\varepsilon,\ \dot{\varepsilon},\ T) = (A + B\varepsilon^{n})(1 + C\ln\dot{\varepsilon}^{*})(1 - T^{*m}) \tag{1}$$

Where σ is plastic stress, ε is the plastic strain, A is the yield stress of the material, B is the strain hardening constant, n is the strain hardening coefficient, C is the strengthening constant of strain rate, m is the thermal softening coefficient, $\dot{\varepsilon}^{*}$ is the dimensionless strain rate, and T^{*} is the homologous temperature. As the thermal effects, strain rate effects and damage are not considered to be in the scope of this paper, only A, B and n constants have been defined, with the other parameters set equal to 0.

2.2. Finite element modelling of lattice structures and impactor

ABAQUS/Explicit Finite Element solver is selected to simulate the impact phenomenon. Individual unit cell geometries were directly modelled in ABAQUS as 3D surfaces having a homogenous thickness as defined by geometric parameters reported in Fig. 1. The unit cells were then meshed using fully integrated 4-noded continuum shell elements with finite membrane strain (S4 elements in ABAQUS) to minimise hourglass effects. The unit cells were periodically repeated in 3D space to generate a metamaterial core. Fig. 2 describes the assembly of the lattice structure comprising of the metamaterial core, top and bottom face sheets having a length L_p, breadth B_p and height H_c, along with the hemispherical impactor. Face sheets are assigned identical material properties as of the metamaterial core as described in Table 1.

Table 1
Johnson-Cook material characterization data for Al5083-H116.

Parameters	Value	Units
Density (ρ)	*2.75E-09*	*t/mm^3*
Young's modulus (E)	*70 000*	*MPa*
Poisson's ratio (ν)	*0.3*	*[-]*
Yield stress (A)	*215*	*MPa*
Plastic hardening parameter (B)	*280*	*MPa*
Plastic hardening component (n)	*0.404*	*[-]*

Additionally, while for D1 and D2 impact directions the lattice structure is modelled as a single body in ABAQUS, for D3 impact direction the top and bottom face sheets were attached to the metamaterial core through Tie constraints, in order to get a structured mesh on the face sheets for improved accuracy. For modelling contact interactions between individual members of the lattice structure and between the top face sheet and the impactor, a general contact behaviour has been applied to all surfaces, with Hard and Frictionless normal and tangential behaviours respectively.

For consistency with the experimental validation conducted later, a rigid and hollow hemispherical impactor of radius R has been placed at the centre of the lattice structure, along the longitudinal symmetry plane. The impactor has been modelled as a rigid surface, since the internal stress distribution is not of interest, with the mass concentrated in its centre point. As to save simulation time, a cost-effective computational model has been considered, with only half of the lattice structure simulated by splitting along the symmetry plane. It must be noted that the model is only symmetric about one midplane. Symmetric boundary conditions have been then applied to the interface of the dividing plane, to address the behaviour of the whole structure.

Table 2 illustrates the boundary conditions selected for both lattice structure and impactor. In particular, the bottom face sheet has been fixed, while the impactor has been set free to move along the global y-direction. A concentrated mass of 12.5 kg has been imposed on the impactor with selected impact velocities of 2 m/s and 5 m/s, resulting in

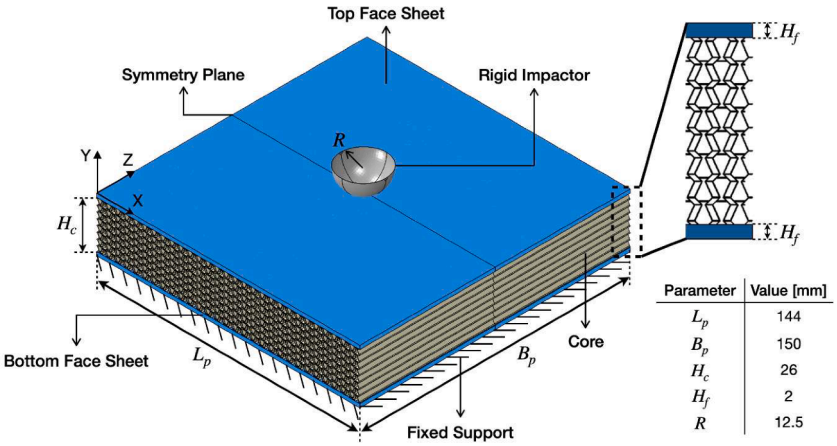

Fig. 2. Isometric view of the metamaterial lattice structure. The metamaterial core, top and bottom face sheets, symmetry plane and their constraints are annotated. Length L_p, breadth B_p, and height H_c values of the lattice structure have been collected in the table inside the image, along with the thickness of the face sheet H_f and impactor's radius R.

Table 2
Boundary conditions for metamaterial lattice structure and impactor.

Impactor constraints	*U1 = U3 = 0; U2 = Free; UR1 = UR2 = UR3 = 0*
Impactor velocity	*V2 = 2 m/s and 5 m/s*
Equivalent impactor mass	*12.5 g*
Bottom face sheet constraints	*U1 = U2 = U3 = UR1 = UR2 = UR3 = 0*

25 J and 156.26 J initial kinetic energies which address therefore the cases of low and high energy impacts.

To select appropriate element sizes for the unit cells, a mesh convergence study was performed by testing both low (2 m/s) and high (5 m/s) impact velocities for the three impact directions. The final mesh sizes selected along with the total number of elements are reported in Table 3. It must be noted that the selected meshes hold validity for both 2 m/s and 5 m/s impact velocities.

To obtain a clear comparison between the performances of the considered metamaterials, all the numerical results have been normalised by the respective structural masses, collected in Table 4.

Appendix A presents the recorded values of hourglass energy error (the ratio of the total artificial strain energy induced in the model and the total energy of the system) for all the models considered [39].

In the next Section 3, results from impact simulations will be presented and a detailed comparison between the behaviour of Fish Cells, Honeycomb, and Re-entrant structures under impact loading is performed. All analyses were conducted on a system equipped with a 6-core Ryzen 3600 CPU paired with 32GB of DDR4 RAM.

3. Discussion of results

In this section, results from the numerical simulations of impact analysis for Fish Cells, Honeycomb, and Re-entrant metamaterial lattice structure are discussed for all considered cases. The parameters investigated for crashworthiness include impactor's penetration depth, von Mises stress distributions, edges deformation and dimensional stability.

Table 3
Mesh sizes and the number of elements for Fish Cells, Honeycomb and Re-entrant lattice structures for impact directions D1, D2 and D3, and for impact velocities of 2 m/s and 5 m/s.

Parameters		Fish Cells	Honeycomb	Re-entrant
Mesh size (mm)	D1	*2.5*	*2*	*3*
	D2	*2.5*	*3*	*3*
	D3	*2.5*	*2*	*3*
Elements number	D1	*171 332*	*55 833*	*41 051*
	D2	*161 901*	*33 351*	*37 851*
	D3	*149 338*	*48 441*	*33 849*

Table 4
Mass for the fish cells, honeycomb and *Re*-entrant lattice structures.

Unit cell geometry	Mass [g]		
	D1	D2	D3
Fish Cells	*226.4*	*220.4*	*211.4*
Honeycomb	*163.9*	*160.3*	*157.9*
Re-entrant	*177.9*	*174.1*	*170.3*

3.1. Impact penetration characteristics and edge deformations

The impactor penetration characteristics and the edge deformations behaviour of the three metamaterial lattice structures are compared for the considered cases of impact velocities of 2 m/s and 5 m/s and impact directions D1, D2 and D3. Fig. 3 illustrates the displacement contour plots for the metamaterial lattice structures for an impact velocity of 2 m/s. Also included in Fig. 3 are key information about the impact crater shape and orientation (expressed by the major axis orientation): it is observed that in all cases the impact crater is strictly localised at the site of impact, with no global edge deformations observed. In particular, Fish Cells and Honeycomb lattice structures in D2, Fig. 3(b, e), exhibit a spherical-shaped crater, signifying isotropic propagation of the deformation in the two planar directions. For the other cases, an ellipsoid-shaped crater whose major axis runs along the z-direction is observed, signifying the non-isotropic propagation of the deformation.

Fig. 4 illustrates the displacement contour plots for the metamaterial lattice structures for an impact velocity of 5 m/s. Here, global edge deformations are observed specifically in the case of Honeycomb D2, Fig. 4(e), and Re-entrant D1 and D2, Fig. 4(g, h), while no global edge deformations are observed in the case of Fish Cells, Fig. 4(a, b, c). It must be noted that the Fish Cells is the only metamaterial lattice structure showing only local deformations and no global edge deformations in all three directions, thus possessing high dimensional stability properties under high velocity impact loading. Fig. 4 also summarises the recorded impact crater shapes for an impact velocity of 5 m/s. It can be noticed how only Fish Cells in D2, Fig. 4(b), shows a spherical crater shape, meaning isotropic propagation of the deformation in the two planar directions. All other geometries present an elliptical shape with a major axis along the z-direction, Fig. 4(a, d, g, e, h), and x-direction, Fig. 4(c, f, i), signifying the non-isotropic propagation of the deformation.

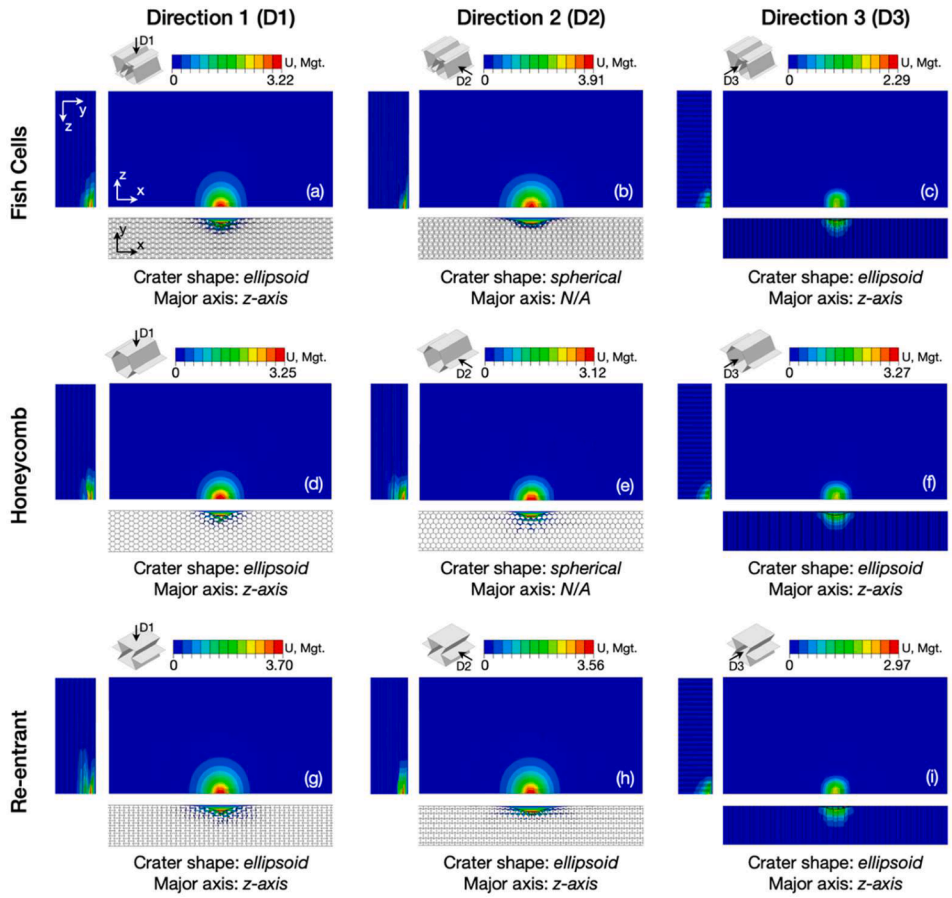

Fig. 3. Displacement contour plots (U, Magnitude) for 2 m/s impact velocity. (a, b, c) Fish Cells, (d, e, f) Honeycomb, (g, h, i) Re-entrant metamaterial lattice structures with impact orientation in direction 1 (a, d, g), direction 2 (b, e, h), and direction 3 (c, f, i). Impact crater shape and related major axis orientation reported for each case. Half lattice structures have been represented.

In the three cases of global edge deformation, it can be noticed how the metamaterial core in Honeycomb D2 converges inwards, while the metamaterial core in Re-entrant D1 and D2 converges outwards. Additionally, in Re-entrant D1 and D2 the deformation is observed to have reached the bottom facesheet, signifying the complete depth of the lattice structure was used to absorb the impact force. Furthermore, for Re-entrant D1 it is observed that the impact has induced twisting in the unit cell members about the x-axis towards the impact crater, signifying compression of the lattice structure along the z-axis. This produces a unique 'flying bird' shape, visible in the x-y shear plane. Finally, for Re-entrant D2 a complete buckling of the array of unit cells in the x-direction is observed where the bottom array collapses first and the buckling propagates towards the top of the metamaterial lattice structure. In this regards, buckling occurs once a critical load is achieved, as is illustrated in the force-displacement plots illustrated in Fig. 5.

Fig. 5 illustrates the mass-normalised force-displacement characteristics for the considered geometries and loading conditions. In all cases the force corresponds to the reaction force recorded at the bottom face sheet, and the values have been normalised by the masses of the respective lattice structures. It is observed that the primary form of deformation and energy absorption for D1 and D2 is core crushing caused by joint deformation between the individual unit cell members, while for D3 it is represented by buckling of unit cells in the direction of extrusion.

Also, compared to D1 and D2, in all cases D3 possesses the highest stiffness which is depicted by relatively higher force and lower penetration depth. This results in higher g-forces being transferred to the bottom face sheet, making it more suitable for applications where penetration depth is a critical factor to prevent damage to critical systems like aircraft wing mechanisms. Furthermore, the area under the force-displacement plots in Fig. 5 represents the energy absorbed by the lattice structures: as an additional result, the relative plots for normalised internal energy absorbed vs time are reported in Fig. B in Appendix B for the considered cases. It must be noted that the total energy absorbed remains the same for all the cases, as all the kinetic energy from the impactor is absorbed by the metamaterial lattice structure. The elastic strain energy of the metamaterial lattice structure is then transferred to the impactor, causing it to rebound. Here, the internal energy (ALLIE) is the sum of artificial energy/hourglass energy (ALLAE), plastic dissipation energy (ALLPD) and elastic strain energy (ALLSE) [39].

In practical applications, geometric configurations of the lattice metamaterial must be selected considering the requirements and desired capabilities of the crash structure, while compromising between parameters of stiffness, available crashable area and g-forces transferred. From the previous simulation, Fig. 6 reports the critical values of normalized penetration depth (mm/kg), Fig. 6(a), normalized peak reaction force (kN/kg), Fig. 6(b), and normalized stiffness (kN/mm*kg), Fig. 7 (which descends from the two graphs in Fig. 6). It should be mentioned that the reaction forces are recorded from the bottom face sheet of the lattice structure and the stiffnesses are calculated as the average slope from the force-displacement plots illustrated in Fig. 5.

It is observed in Fig. 6(a) that Fish Cells allow for the minimum normalised penetration in all considered cases. This makes the Fish Cells lattice structure an ideal candidate for applications where penetration should be minimized such as ballistics protection products including helmets and vests. Also, Fish Cells exhibit the lowest reaction force in D2 impact direction for velocity of 2 m/s, as shown in Fig. 6(b). This characteristic is ideal where transfer of high g-forces to the neighbouring

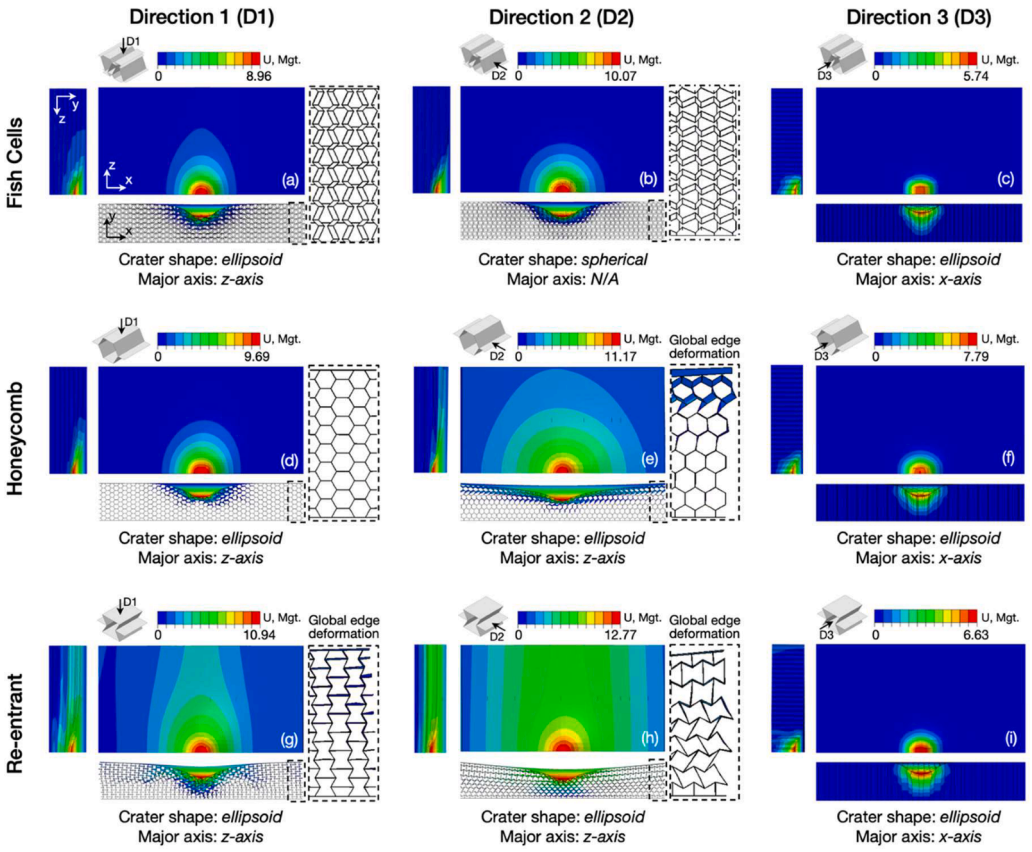

Fig. 4. Displacement contour plots (U, Magnitude) for 5 m/s impact velocity. (a, b, c) Fish Cells, (d, e, f) Honeycomb, (g, h, i) Re-entrant metamaterial lattice structures with impact orientation in direction 1 (a, d, g), direction 2 (b, e, h), and direction 3 (c, f, i). Impact crater shape and related major axis orientation reported for each case, together with indication of eventual global edge defomations. Half lattice structures have been represented.

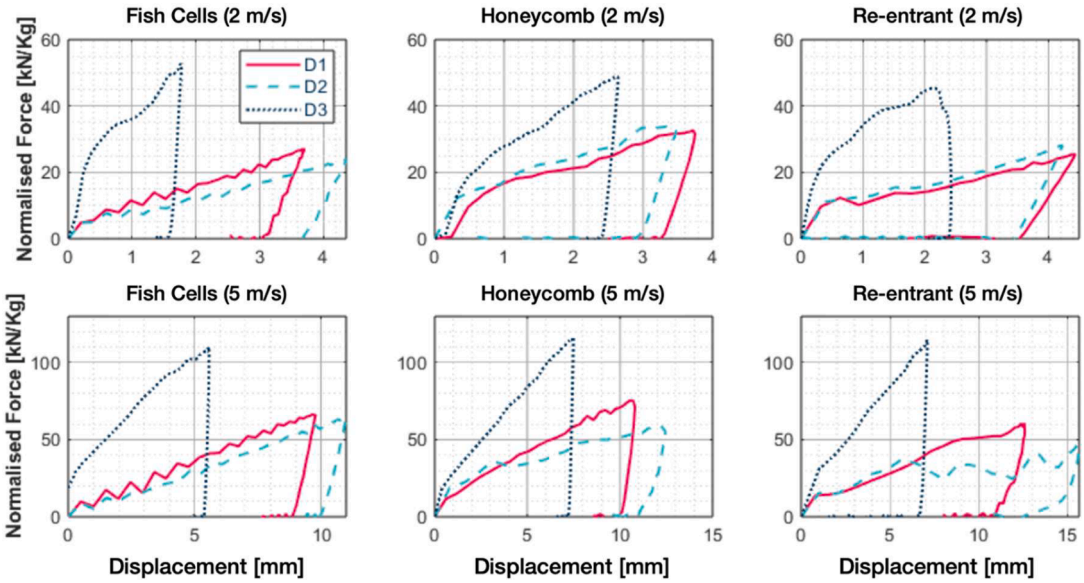

Fig. 5. Mass-normalized impact force vs impactor displacement for impact directions D1, D2, and D3, for Fish Cells lattice structure for an impact velocity of (a) 2 m/s and (b) 5 m/s, for Honeycomb lattice structure with an impact velocity of (c) 2 m/s and (d) 5 m/s and Re-entrant lattice structure with an impact velocity of (e) 2 m/s and (f) 5 m/s.

components is undesirable, for example in the case of a vehicle passenger compartment where a high-rigidity structure is required to protect the passenger from any external intrusions or to avoid the deformation of the passenger compartment itself. The rigid cabin is attached to a purpose-built crash structure that is designed to absorb the impact energy while avoiding high reaction forces to be transferred to the passenger, as to minimize injuries [40]. Other examples include fuselage crash structures of aircrafts and helicopters, or sport protective

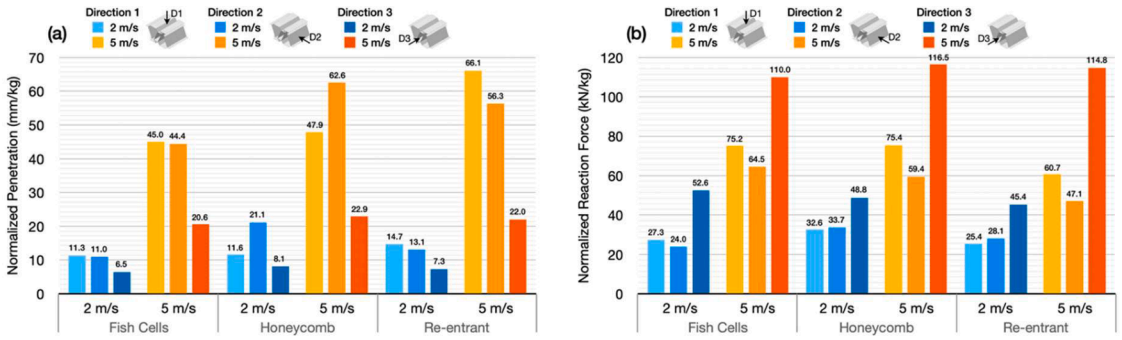

Fig. 6. Comparison of mass-normalised (a) penetration and (b) reaction force for Fish Cells, Honeycomb and Re-entrant lattice structure, for 2 m/s and 5 m/s impact velocities and impact directions D1, D2 and D3.

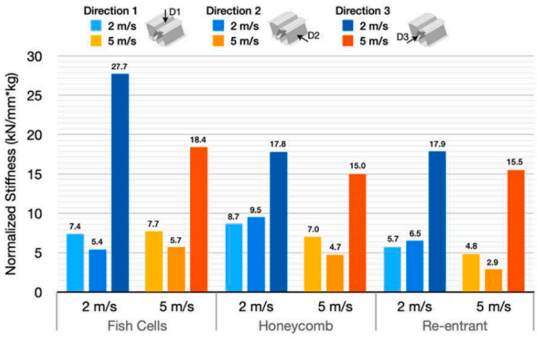

Fig. 7. Comparison of mass-normalised stiffness for Fish Cells, Honeycomb and Re-entrant lattice structure, for 2 m/s and 5 m/s impact velocities and impact directions D1, D2 and D3.

equipment like elbow and knee pads.

Furthermore, as showed in Fig. 7 Fish Cells have the highest stiffness for all impact directions with 5 m/s velocity, whereas for 2 m/s velocity it is highest for D3 direction.

3.2. Von Mises stress distribution

In completion to previous results, the von Mises stress distribution characteristics of the metamaterial lattice structures have been compared for all considered cases. The von Mises stress contour plots of the Fish Cells structure have been collected in Fig. 8. Additionally, Fig. C in Appendix C include the von Mises stress contour plots of Honeycomb and Re-entrant structures. It must be noted that, as the yield strength of the base material used is 215 MPa, any reported value beyond this threshold indicates that the lattice structure has undergone plastic deformation associated with strain hardening, illustrated as grey contours plots in Fig. 8 and Fig. C in Appendix C.

In the 2 m/s impact velocity case, Fig. 8(a, b, c), it can be observed that in D1 and D2 the stress wave magnitude has a relatively lower propagation depth when compared to D3, due to the relatively higher stiffness. Moroever, for the 5 m/s impact velocity case, Fig. 8(d, e, f), it is observed that higher impact velocity directly results in a higher depth of stress wave propagation. For D1 and D2 the stress wave saturated the top face sheet and expanded along the horizontal plane in the z-direction, influencing the boundaries of the lattice structure. In contrast, for D3 the stress wave travels downwards from the impact point towards the bottom face sheet, as observed for the 2 m/s impacts. Furthermore, it must be noted that the Fish Cells lattice structure shows highly localised damaged regions in all impact directions, unlike Honeycomb D2 and Re-entrant D1 and D2 lattice structures. This proves to be an inherent advantage of the Fish Cells design, as it enhances the opportunity of its repairing by cutting out the localised damaged section and replacing it with a new composite core, reducing waste and promoting the

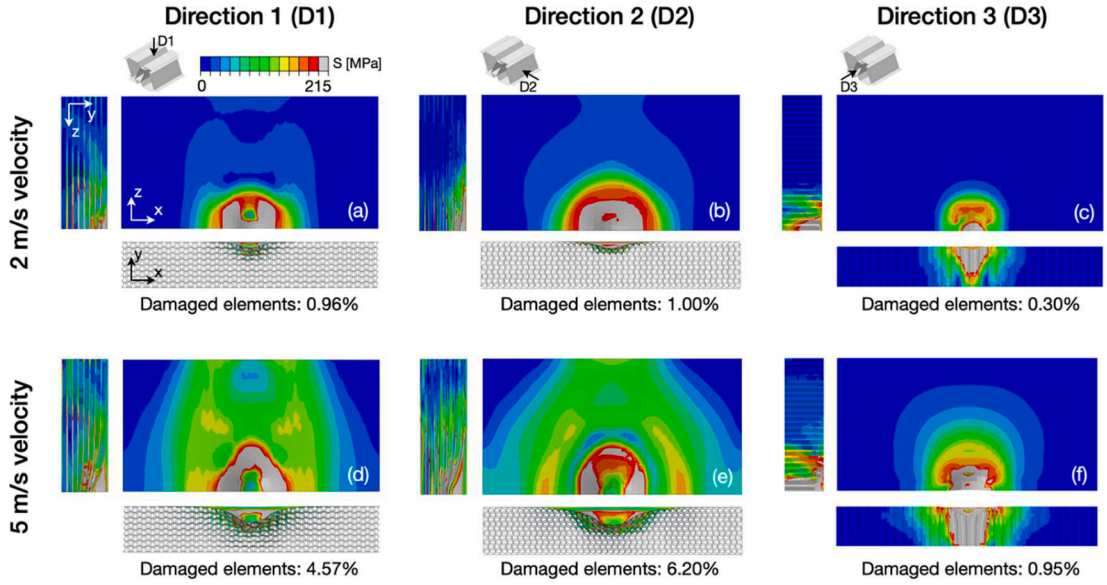

Fig. 8. Von Mises stress contour plots for Fish Cells lattice structure. (a, b, c) Impact velocity of 2 m/s, (d, e, f) impact velocity of 5 m/s. (a, d) Impact orientation in D1, (b, e) D2, (c, f) D3. Stress values have been capped at the base material's yielding value of 215 MPa. Half lattice structures have been represented.

reusability of the affected component. Also included in Fig. 8 and in Fig. C in Appendix C are the percentage of damaged elements. Data have been extracted by analysing the von Mises stress distribution, where any mesh element having stress higher than the yield stress of the constituent material (215 MPa for Aluminium alloy Al5083-H116) is considered completely damaged.

Fig. 9 shows that Fish Cells have the lowest damage ratio in all impact directions for 2 m/s velocity, however for velocity of 5 m/s Fish Cells have the lowest damage ratio in D3 direction. This increases the lifetime of the lattice structures and reduce the repair costs. In situations where penetration is a critical factor, like an aeroplane wing, a high-stiffness lattice structure must be selected to avoid damage to the internal control mechanism.

Furthermore, Appendix D is enriched with Table D wich presents the relative advantages of all geometries from different perspectives. In this regard, the overall advantage of metamaterial lattice structures is related to how their characteristics can be tailored by changing the topology, shape, size of the unit cells, design of joints [41] and hybrid materials to achieve desired crashworthiness characteristics for specific applications.

4. Experimental validation

In this section, experimental validation conducted on the Fish Cells metamaterial lattice structure through a drop tower test setup is presented, and results are discussed. The analysis includes considerations on sizing and unit cell orientations based on manufacturing constraints followed by material characterization. Finally, the results obtained from the experimental analyses are compared to their corresponding numerical models to validate the proposed methodology.

4.1. Material characterization

Experimental validation has been performed using Nylon PA2200 material, instead of Aluminium alloy Al5083-H116, due to ease and reduced cost of manufacturing. Five dog-bone tensile test samples were manufactured through 3D printing with Nylon PA2200 material. The dog-bone samples were then evaluated following ASTM D638–14 standard [42]. These tests were performed using an Instron 5965 tensile test machine equipped with a 5 kN load cell. From the experimental data, the average values of elastic properties and the plastic stress-strain data were calculated as described in Fig. 10. The presented material properties were then incorporated in the Abaqus FE modelling using a piecewise elastic-plastic material model.

4.2. Manufacturing and test setup description

For experimental analysis, only the Fish Cells metamaterial lattice structure has been selected. Fish Cells lattice structures in impact directions D1 and D2 were manufactured by 3D printing using the Selective Laser Sintering (SLS) technique and are shown in Fig. 11(a). Impact direction 3 could not be manufactured due to the physical bed size constraints of the 3D printer.

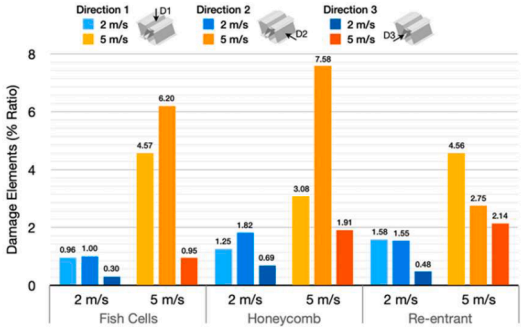

Fig. 9. Comparing element damage ratio for Fish Cells, Honeycomb and Re-entrant lattice structure, for 2 m/s and 5 m/s impact velocities and impact direction D1, D2 and D3.

Additionally, due to manufacturing constraints related to the 3D printer's bed size, some of the lattice structure dimensions were altered. The updated dimensions have been collected in Table 5 for clarity. Tests were performed using the drop tower test setup in the *Cranfield Impact Centre (CIC)* laboratory located at Cranfield University.

Fig. 11(b) illustrates the experimental setup, consisting of the load cell used for measuring the impact force, a laser used for calibration, and a high-speed camera necessary for capturing the deformation mechanism. It must be noted that a stainless steel rigid hemispherical impactor is used along with additional weights to get an impact mass of 12.5 kg. This has been simulated by considering an equivalent concentrated mass of 12.5 kg on the centre of the impactor to maintain consistency of the initial kinetic energy of the system (refer to Section 2.2). Tests were performed with an impact velocity of 5 m/s and a corresponding total initial kinetic energy of the system equal to 156.25 J. Force-displacement curves were captured along with the internal energy of the system, which was calculated by the test machine, and the data were filtered using a standard CFC 180 filter.

A corresponding numerical model has been developed with the same material characterisation (refer to Fig. 10) and geometric parameters (refer to Table 5) as the physical model, with other model parameters such as mesh, section properties, boundary conditions and contact interactions identical to the previously analysed numerical models (refer to Section 2.2).

4.3. Comparison of numerical and experimental models

Fig. 12(a) describes the deformation mechanism at the maximum penetration depth for both impact directions D1 and D2. It is observed that the impactor penetrates the top face sheet going into the core, which is in stark contrast with the deformation mechanism discussed in Section 3. This is because the nylon material used for 3D printing has lower toughness compared to aluminium alloy. This leads to a significant part of the initial kinetic energy being dissipated in the form of tensile and shear failures of the unit cells' individual members. For the aluminium lattice structure discussed in Section 3, instead, the primary form of energy dissipation was the crushing of the lattice structure due to plastic hinge formation at the joint of the unit cells.

Fig. 12(b) compares the force-displacement characteristics, internal energy and kinetic energy of the lattice structures obtained from experimental analysis and numerical simulations. It is observed that the parameters for the numerical and experimental models show a good correlation within tolerable limits, thus validating the proposed approach. Table 6 summarizes the critical points recorded in the plots provided in Fig. 12(b) and presents the percentage error for each case. In particular, the maximum error recorded is 11.57% in the case of D2, while all the other values are equal to or below 5%. It can be noticed how the accuracy of results can be eventually increased by utilising a strain-rate-based material model, which is outside the scope of the present article.

5. Conclusions

In this work, the impact behaviour and crashworthiness of the novel ZPR Fish Cells metamaterial lattice structure has been studied in comparison to well-known PPR Honeycomb and NPR Re-entrant metamaterial lattice structures, considering three different orthogonal impact directions and two different impact velocities of 2 m/s and 5 m/s. In particular, the novel Zero Poisson's Ratio (ZPR) Fish Cells metamaterial has been assembled for the first time as a 3D lattice structure, together with conventional Honeycomb and Re-entrant metamaterials. For consistency of results, the height and length of the three-unit cells

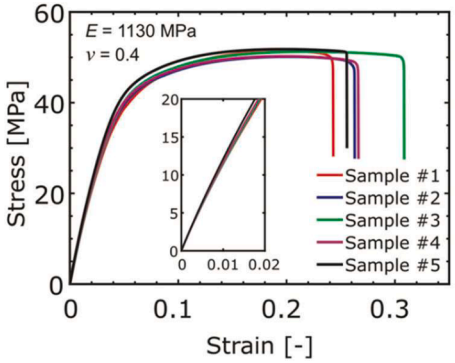

Stress [MPa]	Plastic Strain
14.0	0
34.1	0.025
42.7	0.05
46.7	0.075
49.0	0.1
50.5	0.125
51.3	0.15
51.6	0.175

Fig. 10. Elastic and plastic material properties for Nylon PA2200.

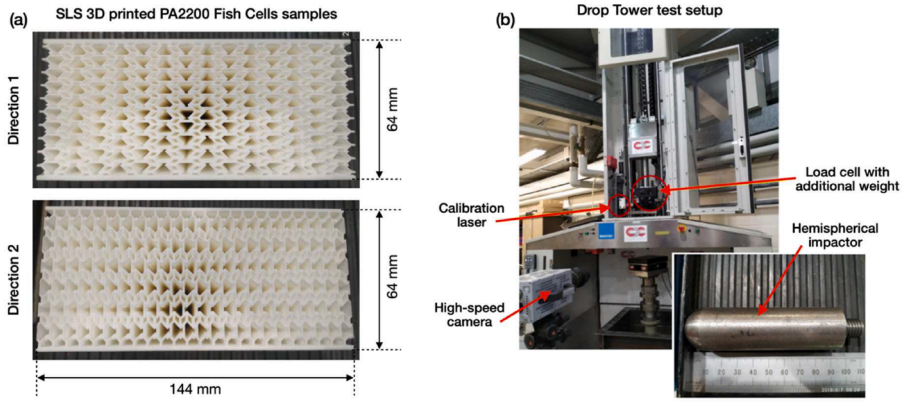

Fig. 11. (a) SLS 3D printed Fish Cells test samples for impact directions D1 and D2, with dimensions annotated; (b) Drop tower test setup, showing the load cell, laser for calibration, high-speed camera, and hemispherical impactor.

Table 5
Lattice structure sizing for manufacturing.

Parameter	Value (mm)
Length of lattice structure (L_p)	144
Breadth of lattice structure (B_p)	100
Height of lattice structure (H_P)	64
Thickness of unit cell (T_c)	1

have been kept constant providing equal unit cell density. The three orthogonal directions considered for impact analyses for each structure were two in-plane (D1 and D2) and one out-of-plane (D3), completely assessing the lattice's dynamic behaviour.

The parameters considered for the numerical analyses were impactor's penetration depth, von Mises stress distribution, edges deformation and damage characteristics. In particular, two unique crater shapes were observed, a spherical one signifying planar isotropic propagation of the deformation, and an ellipse-shaped one implying its non-isotropic propagation. In this regard, it has been observed how the Fish Cells possess strictly localised impact craters with no global edge deformations in all directions of impact and for both impact velocities considered, showing therefore a high degree of dimensional stability. This provides an opportunity to minimize the size of the lattice structure while maintaining the same energy absorption capacity and highlights the superiority of Fish Cells in energy absorption per unit mass.

From the simulation results, it has been observed that the primary

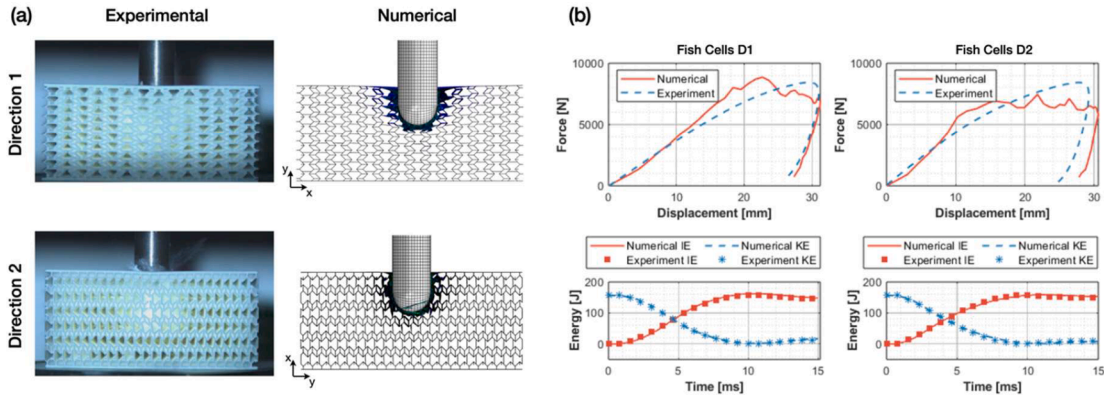

Fig. 12. (a) Comparison of results from the experimental analysis and numerical models for Fish Cells lattice structure deformation in D1 and D2. (b) Force-displacement curves, internal and kinetic energy vs time curves obtained from the experimental and numerical analyses.

Table 6
Critical values from experimental and numerical analyses and recorded % errors.

Parameter	D1			D2		
	Experimental	Numerical	Error [%]	Experimental	Numerical	Error [%]
Max force (N)	*8435.8*	*8857.3*	*5.00*	*8425.6*	*7450.9*	*11.57*
Max penetration (mm)	*31*	*31.24*	*0.77*	*29.24*	*30.6*	*4.75*
Max internal energy (J)	*158.3*	*162.3*	*2.56*	*158.4*	*158.7*	*0.19*
Max kinetic energy (J)	*158.3*	*156.3*	*1.27*	*158.4*	*156.3*	*1.39*

mode of deformation and energy absorption for both D1 and D2 is due to core crushing caused by joint deformation between the individual unit cell members. For D3, instead, the primary deformation mechanism recorded is the buckling of unit cells in the direction of extrusion. Additionally, if compared to D1 and D2, D3 possesses the highest stiffness values which is depicted by relatively higher force and lower penetration depth - results in higher g-forces being transferred to the bottom face sheet. Moreover, Fish Cells lattice structure in D1, D2 and D3 shows highly localised damaged regions, unlike Honeycomb (D2) and Re-entrant (D1 and D2) structures. This provides proof of a structural integrity advantage for the ZPR lattice structure as impact transfer and side effects on neighbouring components are minimised. Also, it proves to be an inherent advantage of the Fish Cells lattice structure, as it enhances reparation opportunities by cutting out the localised damaged section and replacing it with a new composite core, reducing waste and promoting the reusability of the overall structure.

To validate the proposed numerical methodology, an experimental analysis has been performed, involving a drop tower impact test. Such approach has been used to validate the modelling parameters considered for the numerical analyses, by comparing SLS 3D printed Fish Cells lattice structure with their corresponding numerical models, for two impact directions (D1 and D2). The result showed a good correlation between the experimental and numerical data and a maximum error of 11.57% was recorded, thus validating the proposed numerical approach.

Future work is expected to address the limitations of the current research. In particular, the experimental sample used in Section 4 was different, in terms of unit cell's element sizes and material from the numerical model analysed in Section 3 (although a corresponding numerical model has been compared as well to justify the experimental validation process). Moreover, impact direction D3 was not tested, due to manufacturing constraints posed by the 3D printing process, and the 2 m/s velocity was not considered as only limited samples could be manufactured. Furthermore, the choice of manufacturing process posed limitations in areas of panel sizing and choice of materials for manufacturing. A more comprehensive work should focus on all impact scenarios through the research. Nonetheless, the results obtained allowed to conclude on the validation of the numerical models proposed in the work. In addition, further work should focus on testing different impactor shapes and sizes and different boundary conditions (constraints of the metamaterial panel, which in this paper has only been considered encastred to the test bed) to better reproduce a real-life application of the panel. A parametric study including varying Fish Cells densities (number of unit cells per volume) would be beneficial as it provides a further direction of structural optimization. Additional study cases include mixed cells behaviour, represented by the presence of different unit cells inside the same panel and the experimental testing of ballistic impact speeds.

In conclusion, Fish Cells metamaterial lattice structure shows excellent crashworthiness characteristics showing great potential for future application studies: the advantage of ZPR metamaterials unfurls interesting opportunities such as maximising vibration damping and crashworthiness of resilient building or transport infrastructure in the field of civil structural engineering, manufacturing biomaterials and soft robotic medical devices, where tailored stiffness of metamaterials can be used in implants, developing impact-resistant composites, non-pneumatic tyres and aerodynamic morphing spoilers for application in automotive and aerospace industries, developing lattice structure-based sports protective gears. Such varied design requirements can be met by optimising the energy absorption characteristics of the impact lattice structure by changing the density of the unit cell layers, optimising the shape of the unit cell, varying the thickness of the unit cell members, or using combinations of materials and unit cell geometries.

CRediT authorship contribution statement

Ashutosh Jha: Conceptualization, Methodology, Investigation, Writing – original draft. **Guglielmo Cimolai:** Conceptualization, Methodology, Writing – review & editing. **Iman Dayyani:** Methodology, Resources, Writing – review & editing, Supervision.

Declaration of Competing Interest

The authors declare that they have no known competing financial interests or personal relationships that could have appeared to influence the work reported in this paper.

Data availability

Data will be made available on request.

Appendix A

Table A presents the recorded values of hourglass energy error for the metamaterial lattices in D1, D2 and D3 impact directions, with both impact velocities of 2 m/s and 5 m/s considered. This is the ratio of the total artificial strain energy induced in the model and the total energy of the system. Hourglass values below 5% are considered acceptable, especially in the case of fully integrated elements. It can be observed the maximum error percentage recorded is 2.16% for Fish Cells lattice structure for an impact velocity of 5 m/s in D3 impact direction.

Table A
Hourglass energy error % for Fish Cells, Honeycomb and Re-entrant lattice structure for impact directions D1, D2 and D3, and impact velocities of 2 m/s and 5 m/s.

Geometry	2 m/s impact velocity			5 m/s impact velocity		
	D1	D2	D3	D1	D2	D3
Fish Cells	*0.48 %*	*0.86 %*	*1.01 %*	*0.62 %*	*1.01 %*	*2.16 %*

(*continued on next page*)

Table A (*continued*)

Geometry	2 m/s impact velocity			5 m/s impact velocity		
	D1	D2	D3	D1	D2	D3
Honeycomb	*0.92 %*	*0.99 %*	*0.82 %*	*1.14 %*	*0.77 %*	*1.77 %*
Re-entrant	*0.63 %*	*0.69 %*	*0.95 %*	*0.80 %*	*0.79 %*	*2.01 %*

Appendix B

Fig. B

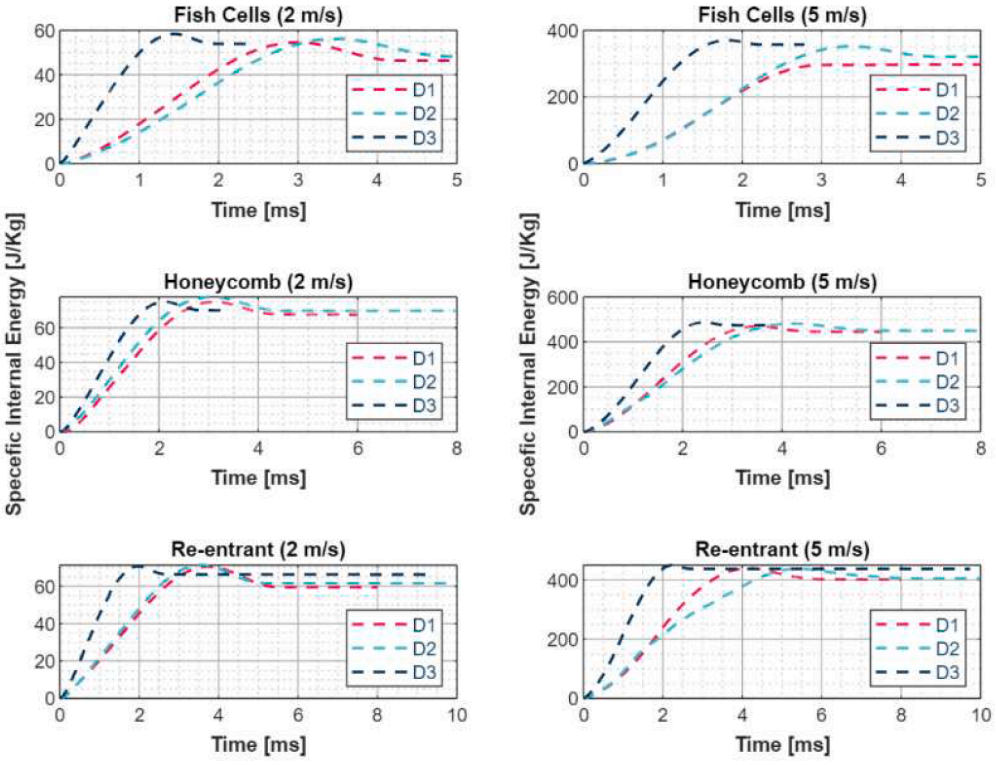

Fig. B. Normalised internal energy vs time for Fish Cells lattice structure for impact orientation in Direction 1 (D1), Direction 2 (D2) and Direction 3 (D3) for impact velocity of (a) 2 m/s and (b) 5 m/s; for Honeycomb lattice structure for impact orientation in Direction 1 (D1), Direction 2 (D2) and Direction 3 (D3) for impact velocity of (c) 2 m/s and (d) 5 m/s; for Re-entrant lattice structure for impact orientation in Direction 1 (D1), Direction 2 (D2) and Direction 3 (D3) for impact velocity of (e) 2 m/s and (f) 5 m/s.

Appendix C

Fig. C

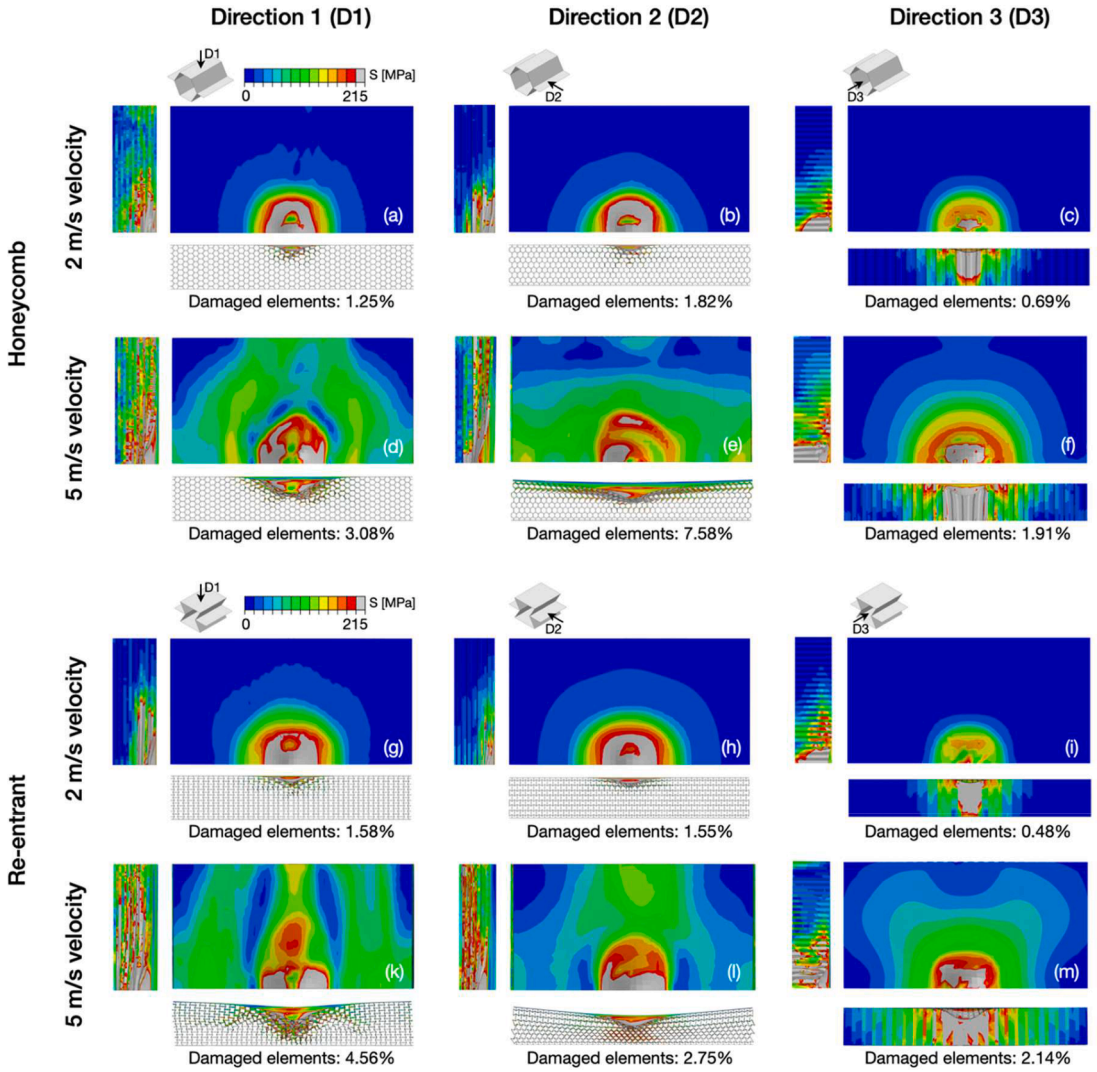

Fig. C. Von Mises stress contour plots for Honeycomb and Re-entrant lattice structures. (a, b, c) Impact velocity of 2 m/s, (d, e, f) impact velocity of 5 m/s, for Honeycomb; (g, h, i) Impact velocity of 2 m/s, (k, l, m) impact velocity of 5 m/s, for Re-entrant. (a, d, g, k) Impact orientation in D1, (b, e, h, l) D2, (c, f, i, m) D3. Stress values have been capped at the base material's yielding value of 215 MPa. Half lattice structures have been represented.

Appendix D

Table D

Table D
Relative differences between lattice structure for mass-normalised penetration depth, reaction force, stiffness, and for damage ratio.

Parameters	Impact directions	Impact velocity (2 m/s)			Impact velocity (5 m/s)		
		Baseline	Relative difference		Baseline	Relative difference	
Normalised penetration depth	*D1*	*Fish Cells*	*Honeycomb* *+2.7 %*	*Re-entrant* *+30.1 %*	*Fish Cells*	*Honeycomb* *+6.4 %*	*Re-entrant* *+46.9 %*
	D2	*Fish Cells*	*Re-entrant* *+19.1 %*	*Honeycomb* *+91.8 %*	*Fish Cells*	*Re-entrant* *+26.8 %*	*Honeycomb* *+41 %*
	D3	*Fish Cells*	*Re-entrant* *+12.3 %*	*Honeycomb* *+24.6 %*	*Fish Cells*	*Re-entrant* *+6.8 %*	*Honeycomb* *+11.2 %*
Normalised reaction force	*D1*	*Honeycomb*	*Fish Cells* *−16.3 %*	*Re-entrant* *−22.1 %*	*Honeycomb*	*Fish Cells* *−0.3 %*	*Re-entrant* *−19.5 %*
	D2	*Honeycomb*	*Re-entrant* *−16.6*	*Fish Cells* *−28.8 %*	*Fish Cells*	*Honeycomb* *−7.9 %*	*Re-entrant* *−30 %*
	D3	*Fish Cells*	*Honeycomb* *−7.2 %*	*Re-entrant* *−13.7 %*	*Honeycomb*	*Fish Cells* *−1.5 %*	*Re-entrant* *−4.4 %*
Normalised stiffness	*D1*	*Honeycomb*	*Fish Cells* *−15 %*	*Re-entrant* *−34.5 %*	*Fish Cells*	*Honeycomb* *−9.1 %*	*Re-entrant* *−37.7 %*

(*continued on next page*)

Table D (*continued*)

Parameters	Impact directions	Impact velocity (2 m/s)			Impact velocity (5 m/s)		
		Baseline	Relative difference		Baseline	Relative difference	
	D2	*Honeycomb*	*Re-entrant*	*Fish Cells*	*Fish Cells*	*Honeycomb*	*Re-entrant*
			−31.6 %	*−43.2 %*		*−17.5 %*	*−49.1 %*
	D3	*Fish Cells*	*Honeycomb*	*Re-entrant*	*Fish Cells*	*Honeycomb*	*Re-entrant*
			−35.4 %	*−37.5 %*		*−18.5 %*	*−15.8 %*
Damage ratio	*D1*	*Fish Cells*	*Honeycomb*	*Re-entrant*	*Honeycomb*	*Re-entrant*	*Fish Cells*
			+23.2 %	*+39.2 %*		*+32.5 %*	*+32.6 %*
	D2	*Fish Cells*	*Re-entrant*	*Honeycomb*	*Re-entrant*	*Fish Cells*	*Honeycomb*
			+35.5 %	*+45.1 %*		*+55.6 %*	*+63.7 %*
	D3	*Fish Cells*	*Re-entrant*	*Honeycomb*	*Fish Cells*	*Honeycomb*	*Re-entrant*
			+35.5 %	*+45.1 %*		*+50.2 %*	*+55.6 %*

References

[1] Nicolaou ZG, Motter AE. Mechanical metamaterials with negative compressibility transitions. Nat Mater 2012;11:608–13.
[2] Mirzaali MJ, Pahlavani H, Yarali E, Zadpoor AA. Non-affinity in multi-material mechanical metamaterials. Sci Rep 2020;10:11488.
[3] Zheng X, et al. Ultralight, ultrastiff mechanical metamaterials. Science 2014;344:1373–7.
[4] Kadic M, Bückmann T, Stenger N, Thiel M, Wegener M. On the practicability of pentamode mechanical metamaterials. Appl Phys Lett 2012;100:191901.
[5] Chen Y, Li T, Scarpa F, Wang L. Lattice metamaterials with mechanically tunable Poisson's ratio for vibration control. Phys Rev Appl 2017;7:024012.
[6] Grima JN, Oliveri L, Attard D, Ellul B, Gatt R, Cicala G, et al. Hexagonal honeycombs with zero Poisson's ratios and enhanced stiffness. Adv Eng Mater 2010;12:855–62.
[7] Sanami M, Ravirala N, Alderson K, Alderson A. Auxetic materials for sports applications. Procedia Eng 2014:453–8.
[8] Gibson LJ, Ashby MF. Cellular solids: structure and properties. Cambridge university press; 1999.
[9] Bitzer T. Honeycomb technology: materials, design, manufacturing, applications, and testing. Springer Science & Business Media; 2012.
[10] Alderson A, Alderson KL, Chirima G, Ravirala N, Zied KM. The in-plane linear elastic constants and out-of-plane bending of 3-coordinated ligament and cylinder-ligament honeycombs. Compos Sci Technol 2010;70(7):1034–41.
[11] Evans KE. The design of doubly curved sandwich panels with honeycomb cores. Compos Struct 1991;17(2):95–111.
[12] Liu L, Meng P, Wang H, Guan Z. The flatwise compressive properties of Nomex honeycomb core with debonding imperfections in the double cell wall. Compos B Eng 2015;76(Supplement C):122–32.
[13] Sun Z, Shi S, Guo X, Hu X, Chen H. On compressive properties of composite sandwich structures with grid reinforced honeycomb core. Compos B Eng 2016;94(Supplement C):245–52.
[14] Wang Z, Liu J, Hui D. Mechanical behaviors of inclined cell honeycomb structure subjected to compression. Compos B Eng 2017;110(Supplement C):307–14.
[15] Tao Y, Duan S, Wen W, Pei Y, Fang D. Enhanced out-of-plane crushing strength and energy absorption of in-plane graded honeycombs. Compos B Eng 2017;118(Supplement C):33–40.
[16] Ren W, McMullan PJ, Griffin AC. Poisson's ratio of monodomain liquid crystalline elastomers. Macromol Chem Phys 2008;209:1896–9.
[17] Liu J, Zhang Y. A mechanics model of soft network materials with periodic lattices of arbitrarily shaped filamentary microstructures for tunable Poisson's ratios. J Appl Mech 2018:85.
[18] Yang H, Ma L. Multi-stable mechanical metamaterials with shape-reconfiguration and zero Poisson's ratio. Mater Des 2018;152:181–90.
[19] Nagavi Zadeh M, Dayyani I, Yasaee M. Fish Cells, a new zero Poisson's ratio metamaterial—part I: design and experiment. J Intell Mater Syst Struct 2020;31(13):1617–37.
[20] Lim TC. Auxetic materials and structures. Springer; 2014.
[21] Milton GW. Composite materials with Poisson's ratios close to -1. J Mech Phys Solid 1992;40(5):1105–37.
[22] Subramani P, Rana S, Ghiassi B, Fangueiro R, Oliveira DV, Lourenco PB, et al. Development and characterization of novel auxetic structures based on re-entrant hexagon design produced from braided composites. Compos B Eng 2016;93(Supplement C):132–42.
[23] Jin X, Wang Z, Ning J, Xiao G, Liu E, Shu X. Dynamic response of sandwich structures with graded auxetic honeycomb cores under blast loading. Compos B Eng 2016;106(Supplement C):206–17.
[24] Hou Y, Neville R, Scarpa F, Remillat C, Gu B, Ruzzene M. Graded conventional-auxetic Kirigami sandwich structures: flatwise compression and edgewise loading. Compos B Eng 2014;59(Supplement C):33–42.
[25] Chen Y, Scarpa F, Remillat C, Farrow I, Liu Y, Leng J. Curved Kirigami SILICOMB cellular structures with zero Poisson's ratio for large deformations and morphing. J Intell Mater Syst Struct 2014;25(6):731–43.
[26] Bodaghi M, Serjouei A, Zolfagharian A, Fotouhi M, Rahman H, Durand D. Reversible energy absorbing meta-sandwiches by FDM 4D printing. Int J Mech Sci 2020;173:105451.
[27] Lu G, Yu T. Energy absorption of structures and materials. Amsterdam: Elsevier; 2003.
[28] Svensson E. Material characterization of 3D-printed energy-absorbent polymers inspired by nature. Sweden: Chalmers tekniska högskola; 2017.
[29] Sun S, An N, Wang G, Li M, Zhou J. Snap-back induced hysteresis in an elastic mechanical metamaterial under tension. Appl Phys Lett 2019;115:091901.
[30] Sarvestani HY, Akbarzadeh AH, Niknam H, Hermenean K. 3D printed architected polymeric sandwich panels: energy absorption and structural performance. Comp Struct 2018;200:886–909.
[31] Tan X, Chen S, Zhu S, Wang B, Xu P, Yao K, Sun Y. Reusable metamaterial via inelastic instability for energy absorption. Int J Mech Sci 2019;155:509–17.
[32] Zadpoor AA. Additively manufactured porous metallic biomaterials. J Mater Chem B 2019;7:4088–117.
[33] Bates SRG, Farrow IR, Trask RS. 3Dprinted polyurethane honeycombs for repeated tailored energy absorption. Mater Des 2016;112:172–83.
[34] Habib FN, Iovenitti P, Masood SH, Nikzad M. In-plane energy absorption evaluation of 3D printed polymeric honeycombs. Virtual Phys Prototyp 2017;12:117–31.
[35] Sarvestani HY, Akbarzadeh AH, Niknam H, Hermenean K. 3D printed architected polymeric sandwich panels: energy absorption and structural performance. Compos Struct 2018;200:886–909.
[36] Xu M, Xu Z, Zhang Z, Lei H, Bai Y, Fang D. Mechanical properties and energy absorption capability of AuxHex structure under in-plane compression: theoretical and experimental studies. Int J Mech Sci 2019;159:43–57.
[37] Namvar N, Zolfagharian A, Vakili-Tahami F, Bodaghi M. Reversible energy absorption of elasto-plastic auxetic, hexagonal, and AuxHex structures fabricated by FDM 4D printing. Smart Mat Struct 2022;31(5):055021.
[38] Johnson GR, Cook WH. A constitutive model and data for metals subjected to large strains, high strain rates and high temperatures. In: Proc. 7th Int. Symp. Ballist; 1983. p. 541–7.
[39] Dassault Systemes. ABAQUS/CAE user's guide. Providence RI, USA: Dassault Systemes Simulia Corp; 2014.
[40] Malen DE. Fundamentals of automobile body structure design, 394. SAE Technical Paper; 2011.
[41] Jha A, Dayyani I. Shape optimisation and buckling analysis of large strain zero Poisson's ratio fish-cells metamaterial for morphing structures. Comp Struct 2021;268:113995.
[42] ASTM International. ASTM D638-14, standard test method for tensile properties of plastics. ASTM International; 2015.

2023-11-03

Crashworthiness and dimensional þÿstability analysis of zero Pois fish cells lattice structures

Jha, Ashutosh

Elsevier

Jha A, Cimolai G, Dayyani I. (2024) Crashworthiness and dimensional stability analysis of zero þÿPoisson s ratio fish cells lattice structures, International Journal of Imp 184, February 2024, Article Number 104809

https://doi.org/10.1016/j.ijimpeng.2023.104809